Analysis of phase front structures for energetic materials

2006 J. Phys.: Condens. Matter 18 8179

(http://iopscience.iop.org/0953-8984/18/35/006)

INSTITUTE OF PHYSICS PUBLISHING JOURNAL OF PHYSICS: CONDENSED MATTER

J. Phys.: Condens. Matter **18** (2006) 8179–8193 doi:10.1088/0953-8984/18/35/006

Analysis of phase front structures for energetic materials

Jack Jai-ick Yoh

School of Mechanical and Aerospace Engineering, Seoul National University, Seoul 151-742, Korea

E-mail: jjyoh@snu.ac.kr

Received 13 May 2006, in final form 18 July 2006
Published 15 August 2006
Online at stacks.iop.org/JPhysCM/18/8179

Abstract

The structure of a steady wave system is considered which is admitted by the continuum equations for materials that undergo phase transformations with exothermic chemical reaction. In particular, the dynamic phase front structures between liquid and gas phases and solid and liquid phases are computationally investigated. With its theoretical basis in one-dimensional continuum shock structure analysis, the present approach estimates the micro-width of waves associated with phase transformation phenomena. For illustration purposes, n-heptane is used in the evaporation and condensation analysis and HMX is used in the melting and freezing analysis of energetic materials of interest. The estimated thickness of the evaporation–condensation front of n-heptane is on the order of 10^{-2} μm while the HMX melting–freezing front thickness is estimated at 1 μm. The present structure analysis is being extended to account for a broader range of energetic materials whose phase front thickness measurements are neither available nor experimentally attainable.

1. Introduction

In the continuum theory, shock is interpreted as a thin region rather than a discontinuity in which rapid changes of the flow quantities occur. Two uniform end states of a typical shock are related through a smooth structure of finite length in microns where the conservation of mass, momentum and energy is achieved [1–3]. In this paper, a new method of estimating the thickness of a wavefront associated with phase transformations that propagates in much the same way as a shock wave in a continuous media is presented.

There have been many papers on the discussion of shock wave structure using both continuum and kinetic theoretical ways of viewing the problem. In the late 1950s, the solution of the Navier–Stokes (NS) model of the continuum was analysed with great detail. The essence of the results obtained with the NS model as summarized in [4] is that its validity is satisfactory for realistic fluids for Mach number up to 1.8. For fluids of Mach number greater than 2, a

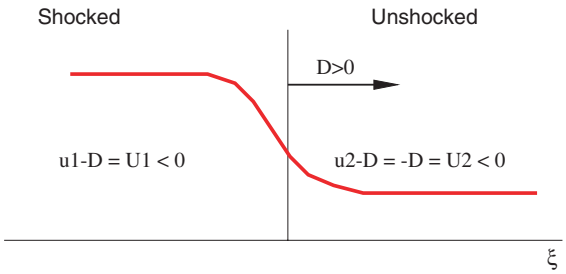

Figure 1. Schematic of shock-attached frame.
(This figure is in colour only in the electronic version)

different approach was necessary. The solution of Boltzmann's equation describing the time evolution of a dilute gas gained much interest after the NS model of the continuum. The direct simulation Monte Carlo (DSMC) method is used to solve that equation. The solution in the hydrodynamic regime is equivalent to the NS model, except that the transport coefficients are obtained in terms of molecular parameters characteristic of each gas. Ruggeri in [5] showed that the solution to the NS model's upper limit (Mach no. < 2) does not exist. For a simple dilute gas, the full nonlinear Burnett equations of hydrodynamics as they appear from the Chapman–Enskog solution to the Boltzmann equation showed that the shock wave profiles in Mach number greater than or equal to two are significantly improved. Amongst different ways of viewing shocks, the continuum approach has gained much interest for propagating interfaces in a simple dilute gas.

Along the line of computing the structure of hydrodynamic shock waves in fluids for a wide range of Mach numbers, we develop an innovative method for analysing the structure of phase fronts in the sense of melting (or freezing) and vaporization (or condensation) between two thermodynamic phases. The analysis of the phase wave profile is based on the theoretical model for energetic materials that was first introduced in [6, 7] where the thermo-mechanical model is derived for a material that experiences phase changes and possible exothermic chemical reaction. A unique feature of the model is that an extra field variable φ is introduced in the time evolution equations so that the current phase of materials considered is automatically determined as a part of the state variables. This phase field approach eliminates the need for cumbersome interface balancing between the two phases. The global treatment of the phase field is the key in this work, where we handle the material phase fronts like the hydrodynamic shock waves and apply the structure analysis to the phase front thickness estimation for the condensed matter, namely an energetic liquid or solid fuel.

In this paper, the liquid–vapour interface is considered that represents the boundary between evaporation and condensation for the hydrocarbon liquid fuel. The phase front of the solid–liquid interface is also analysed for a typical solid explosive. An n-heptane and an HMX are used in the illustration of profiling the phase wave structures.

2. Preliminary

The shocked state is the unstable equilibrium. The integration of the structure starts from this point to a stable point of the unshocked state. Figure 1 shows a steady shock coordinate where $\xi = x - Dt, U = u - D$ and velocities both upstream and downstream are negative, pointing left. Here D is the steady wave speed, directed in the negative ξ direction (i.e. $D < 0$). The

derivatives with respect to x and t become

$$\frac{\partial}{\partial t} = \frac{\partial \xi}{\partial t}\frac{\mathrm{d}}{\mathrm{d}\xi} = -D\frac{\mathrm{d}}{\mathrm{d}\xi}; \qquad \frac{\partial}{\partial x} = \frac{\mathrm{d}}{\mathrm{d}\xi} \tag{1}$$

and the velocity gradient becomes

$$\frac{\partial u}{\partial x} = \frac{\mathrm{d}U}{\mathrm{d}\xi}. \tag{2}$$

Thus the equations of motion for the ideal gas are obtained as follows:

$$\rho U = m, \qquad (U = D - u) \tag{3}$$

$$\frac{\mathrm{d}U}{\mathrm{d}\xi} = \frac{3}{4\mu_f}\left\{mU_{-\infty} + \frac{m}{U_{-\infty}}RT_1 - mU - \frac{m}{U}RT\right\} \tag{4}$$

$$\frac{\mathrm{d}T}{\mathrm{d}\xi} = \frac{1}{\kappa}\left\{\frac{\gamma}{\gamma-1}mRT_1 + \frac{1}{2}mU_{-\infty}^2 - \frac{4}{3}\mu_f U U_\xi - \frac{\gamma}{\gamma-1}mRT - \frac{1}{2}mU^2\right\} \tag{5}$$

where $m = \rho U$ and $p = \rho RT$. Using the standard constants of air (e.g. $\mu_f = 1.95 \times 10^{-5}$ N s m^{-2}, $\gamma = 1.4$, $\kappa = 0.0276$ W m^{-1} K^{-1}, and $R = 287$ m^2 s^{-2} K^{-1}), one can integrate from a shocked state into an unshocked state or the quiescent ambience.

In the sections that follow, the governing equations for energetic materials that may undergo phase transformations are reviewed. Then the wave thickness associated with propagating melting–freezing or evaporation–condensation phase fronts are calculated in much the same way as in the classical shock structure analysis discussed in this section. With careful handling of these structure equations with accurate material parameters, a sensible estimation of the micro-scale phase front thickness is obtained by this method.

3. Review of governing equations for energetic materials

In [6, 7], a three-dimensional model was derived for energetic materials whose state variables represent the change of phase from solid to liquid to gas. Since the derivation based on the classical thermomechanics is general for a material whose material properties are known, the governing equations can represent various kinds of energetic materials of one's interest. The one-dimensional equations for classical energetic material with three possible phases (solid, liquid, gas) are described here:

$$\frac{\partial \rho}{\partial t} + u\frac{\partial \rho}{\partial x} + \rho\frac{\partial u}{\partial x} = 0 \tag{6}$$

$$\rho\left(\frac{\partial u}{\partial t} + u\frac{\partial u}{\partial x}\right) = \frac{\partial}{\partial x}\left\{\mu_s F - \mu_s F^{\frac{-1}{1-2\nu}} - \rho RT - \rho\gamma_\varphi\left(\frac{\partial \varphi}{\partial x}\right)^2 - \alpha_c\kappa(T - T_0)F^{-1} + \frac{4}{3}\mu_f\frac{\partial u}{\partial x}\right\} \tag{7}$$

$$\frac{\partial F}{\partial t} = \frac{\partial u}{\partial x}F \tag{8}$$

$$\rho c_v\left(\frac{\partial T}{\partial t} + u\frac{\partial T}{\partial x}\right) = \kappa\frac{\partial^2 T}{\partial x^2} + \frac{4}{3}\mu_f\left(\frac{\partial u}{\partial x}\right)^2 - \left(\alpha_c\kappa F^{-1}T + \rho RT\right)\frac{\partial u}{\partial x} + T\rho\left(\beta'_m\frac{Q_m}{T_m} + \beta'_v\frac{Q_v}{T_v}\right)\left(\frac{\partial \varphi}{\partial t} + u\frac{\partial \varphi}{\partial x}\right) + B_\varphi\left(\frac{\partial \varphi}{\partial t} + u\frac{\partial \varphi}{\partial x}\right)^2 \tag{9}$$

$$B_\varphi\left(\frac{\partial\varphi}{\partial t}+u\frac{\partial\varphi}{\partial x}\right)=\frac{\partial}{\partial x}\left(\rho\gamma_\varphi\frac{\partial\varphi}{\partial x}\right)$$
$$-\mu_s'(\varphi)\frac{1}{2}F^{-1}\left(F^2-1\right)$$
$$-\mu_c'(\varphi)\frac{1-2\nu_s}{2\nu_s}F^{-1}\left(F^{\frac{-2\nu_s}{1-2\nu_s}}-1\right)-\mu_l'\frac{3}{2}F^{-1/3}$$
$$+\rho c_v'(\varphi)\left(T\ln\frac{T}{T_0}-(T-T_0)\right)$$
$$-\rho\frac{1}{2}\Psi\frac{\partial}{\partial\varphi}\left(\{(\varphi)(\varphi-1)(\varphi-2)\}^2\right)$$
$$-\rho\beta_m'(\varphi)\frac{T-T_m}{T_m}Q_m-\rho\beta_v'(\varphi)\frac{T-T_v}{T_v}Q_v. \tag{10}$$

Here ρ is the mass density, F the deformation gradient, and φ the phase-field variable. These equations represent the balance laws for conservation of mass, momentum, deformation, energy, and phase-field in order. The variable φ is normalized in such a way that $\varphi = 0$ corresponds to a solid, $\varphi = 1$ a liquid, and $\varphi = 2$ a gas. In the regions where the phase is pure (i.e. $\varphi = 0$, 1, or 2) the material properties and the constitutive relations must describe the pure material with the properties of that phase. For clarity in the phase structure analysis, the exothermic chemical reaction element from the original equations in [6] is already suppressed in the present discussion.

As in the classical shock structure analysis, one-dimensional equations are sufficient for illustrating the structure of phase front profiles for materials that undergo phase transformation. In this work, both liquid and solid forms of energetic materials are considered to describe a basic methodology for obtaining phase front profiles.

3.1. Material transition functions

The important element of the master equations derived in equations (6)–(10) is the use of φ-dependent material properties or the material transition functions. Their most prominent use is in defining the sources of the φ-evolution equation and the energy (temperature) equation. The functions $\mu_c(\varphi)$, $\mu_s(\varphi)$, $\mu_l(\varphi)$, $\alpha_c(\varphi)$, $R(\varphi)$, and $c_v(\varphi)$ all change with the phase variable φ. These functions are defined in such a way that they take on the relevant values for each phase (solid, liquid, gas) of a material. The φ-dependent material transition functions are made of simple, smooth, or piece-wise smooth polynomials of φ as summarized in the appendix.

4. Structure of phase front

Two uniform end states of a typical phase front are related through a smooth structure of finite length in a fraction of a micron where the conservation of mass, momentum, and energy is achieved. Resembling the classical shock structure of a dilute gas, the evaporation–condensation front and melting–freezing front are considered for the two uniform end states.

4.1. Evaporation and condensation front ($1 < \varphi < 2$)

The detailed wave structure between the end states at $\pm\infty$ is obtained by transforming the unsteady flow equations to the steady equations in a frame of reference moving with the wave using $\xi = x - Dt, U = u - D$. Here D is the steady phase front 'wave' speed, directed in

the negative ξ direction (i.e. $D < 0$). The derivatives with respect to x and t and the velocity gradient $\partial u/\partial x$ are defined as before (see equations (1) and (2)).

The mass and momentum equations transform as

$$\rho U = m \tag{11}$$

$$\rho U \frac{\mathrm{d}U}{\mathrm{d}\xi} = \frac{\mathrm{d}}{\mathrm{d}\xi}\left(\sigma + \frac{4}{3}\mu_f \frac{\mathrm{d}U}{\mathrm{d}\xi}\right) \tag{12}$$

where the stress term is defined, $\sigma = -\rho RT - \rho\gamma_\varphi(\frac{\partial\varphi}{\partial x})^2$. It is natural to set $F = 0$ in the governing equations for liquid or gas to reflect the zero deformation condition for the corresponding phases.

Since the structure of a wave is considered, the momentum equation is integrated with respect to ξ, which results in a first-order ODE,

$$mU - \sigma - \frac{4}{3}\mu_f \frac{\mathrm{d}U}{\mathrm{d}\xi} = \beta \tag{13}$$

where β is a constant of integration which is evaluated by letting ξ approach $-\infty$. With mass flux defined constant m, the structure momentum equation reads

$$\frac{\mathrm{d}U}{\mathrm{d}\xi} = \frac{3}{4\mu_f}\left\{mU + p + \rho\gamma_\varphi G^2 - mU_k - p_k\right\} \tag{14}$$

where $G = \frac{\mathrm{d}\varphi}{\mathrm{d}\xi}$. k denotes the far end conditions where k equals 1 for evaporation and 2 for condensation.

As for the energy and phase-field structure equations, the partials with respect to x and t are replaced with derivatives in ξ, and the total derivative $\dot{\phi}$ transforms to $U\frac{\mathrm{d}\phi}{\mathrm{d}\xi}$ where ϕ is either T or φ. Here the specific heat is considered constant with respect to phase variable φ and thus c_v' terms drop out from the governing equations. Now, the energy equation is written with its highest derivative in the first order with a new variable H:

$$\frac{\mathrm{d}H}{\mathrm{d}\xi} = \frac{1}{\kappa}\left\{mc_v H - \frac{4}{3}\mu_f\left(\frac{\mathrm{d}U}{\mathrm{d}\xi}\right)^2 + \rho RT\frac{\mathrm{d}U}{\mathrm{d}\xi} - B_\varphi(UG)^2 - \rho T\beta_v'(\varphi)\frac{Q_v}{T_v}UG + \beta_v'(\varphi)Q_k\right\} \tag{15}$$

where $H = \frac{\mathrm{d}T}{\mathrm{d}\xi}$. A temperature driving term $\beta_v'(\varphi)Q_k$ is added to raise the temperature beyond the vaporization temperature.

As for the phase equation, the governing equation reads

$$\frac{\mathrm{d}G}{\mathrm{d}\xi} = \frac{1}{\gamma_\varphi}\left\{\frac{UB_\varphi G}{\rho} + \frac{1}{2}\Psi\frac{\partial}{\partial\varphi}\{(\varphi(\varphi-1)(\varphi-2))^2\} + \beta_v'(\varphi)\frac{T-T_v}{T_v}Q_v\right\}. \tag{16}$$

Note the dependence of R and β_v on φ. This φ-dependence of the transfer functions noted earlier conforms the structure of waves associated with classical phase transformations. Table 1 summarizes the properties of n-heptane used in the present calculation.

The integration scheme for the resulting autonomous ODEs in ξ is the high-order Runge–Kutta scheme outlined in [10]. In the case of evaporation, the liquid state at $k = 1$

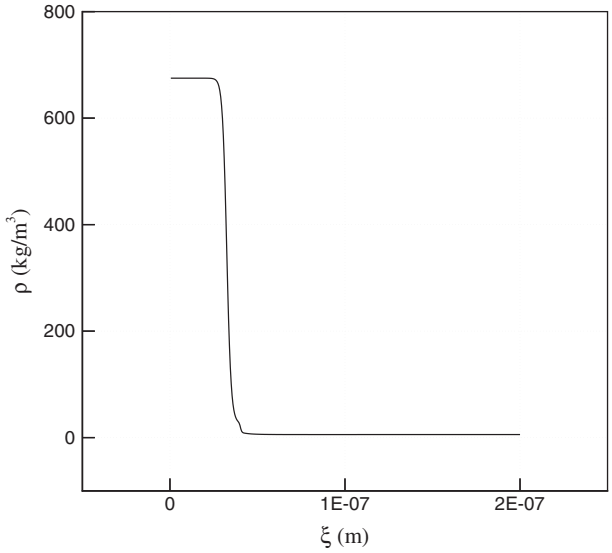

Figure 2. Evaporation wave (liquid $\varphi = 1 \rightarrow$ vapour $\varphi = 2$) structure based on the transformed density field of n-heptane.

Table 1. Dimensional parameters for n-heptane evaporation/condensation [8, 9].

Property	Units	Value
Specific heat—liquid, c_v^{liq}	J kg^{-1} K^{-1}	2.136×10^3 [a]
Specific heat—vapour, c_v^{vap}	J kg^{-1} K^{-1}	2.136×10^1 [b]
Gas constant per unit mass, R_{liq}	J kg^{-1} K^{-1}	3.0×10^2 [c]
Gas constant per unit mass, R_{vap}	J kg^{-1} K^{-1}	3.0×10^2 [a]
Viscosity coefficient, μ_f	kg m^{-1} s^{-1}	5.4×10^{-4} [a]
Multiplication factor of $\dot{\varphi}$, B_φ	kg m^{-1} s^{-1}	3.5×10^{-2} [c]
Phase diffusion coefficient, γ_φ	m kg s^{-2}	2.0×10^{-12} [c]
Depth of phase well, Ψ	J kg^{-1}	40.0×10^{-6} [a]
Vaporization temperature, T_v	K	371.4 [b]

[a] Reference [8].
[b] Reference [9].
[c] Modelled.

(i.e. $\xi = -\infty$) is fixed with the following set of quantities.

$$\left.\begin{aligned} &\rho_1 = 675 \text{ kg m}^{-3} \\ &m = 0.731\,5515 \text{ kg m}^{-2} \text{ s}^{-1} \\ &D = 1.083\,78 \times 10^{-3} \text{ m s}^{-1} \\ &u_1 = 0 \text{ m s}^{-1} \\ &T_1 = 300 \text{ K} \\ &p_1 = 6.075\,00 \times 10^5 \text{ Pa} \\ &\varphi_1 = 1.000\,0001 \\ &H = G = 0 \\ &Q_1 = +3.35 \times 10^{15} \text{ J} \end{aligned}\right\} \xi = -\infty.$$

The numerical integration begins from state 1 (liquid side) at $-\infty$ to a state 2 (gas side) at $+\infty$. Figures 2–4 represent the structure of the evaporation wave admitted by the equations. As the

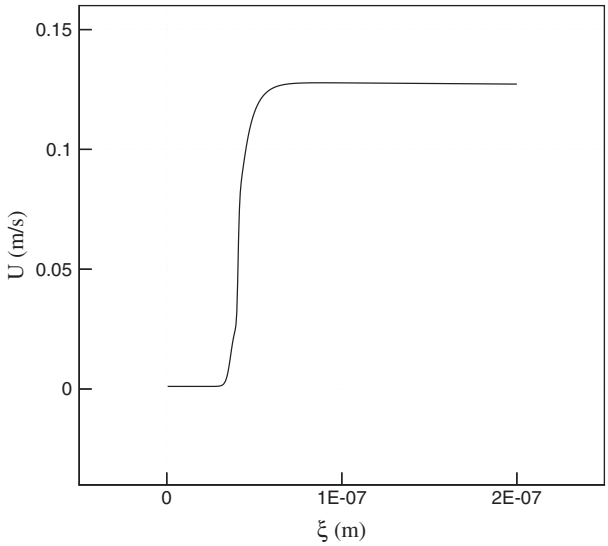

Figure 3. Evaporation wave (liquid $\varphi = 1 \rightarrow$ vapour $\varphi = 2$) structure based on the transformed velocity field of n-heptane.

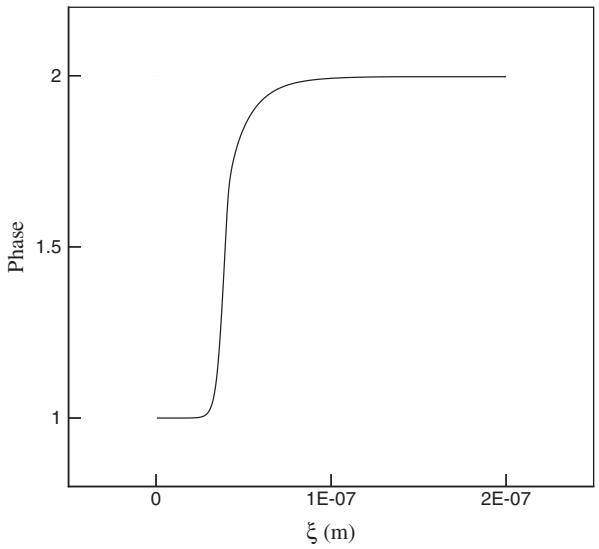

Figure 4. Evaporation wave (liquid $\varphi = 1 \rightarrow$ vapour $\varphi = 2$) structure based on the transformed phase field of n-heptane.

initial state is perturbed, the solution of the structure equation is described by the integration path, going through a particular structure-stable point on the far right side.

The velocity profile in figure 3 shows that the initial value (10^{-3} m s^{-1}) experiences a sudden increase (10^{-1} m s^{-1}) at a structure-stable position where the density jump (in figure 2) is consistent with the experimental evidence for an n-heptane evaporation [11–13]. The thickness of the evaporation wavefront as observed from these figures is on the order of ten nanometres.

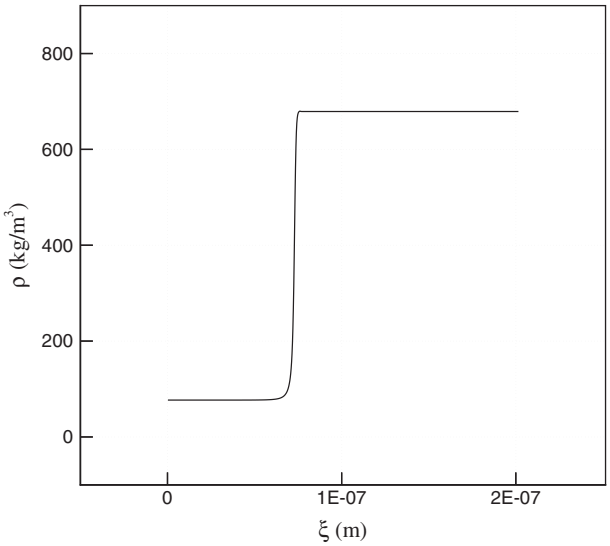

Figure 5. Condensation wave (vapour $\varphi = 2 \rightarrow$ liquid $\varphi = 1$) structure based on the density field of n-heptane.

Considering an experimental thickness measurement of similar waves in helium on the orders of millimetres [14], the suggested evaporation front thickness is much smaller. At each end, the temperature gradient is uniform so that $T(-\infty)$ is a constant and $T(+\infty)$ is linear with respect to ξ, representing a far-field constant thermal-gradient condition for the evaporation process.

In the case of condensation, vapour state 2 is fixed at $-\infty$ as the integration marches along the liquid side at $+\infty$. The initial conditions of integration for condensation are as follows:

$$\left.\begin{array}{l} \rho_2 = 5 \text{ kg m}^{-3} \\ U_2 = 0.11 \text{ m s}^{-1} \\ m = 0.731\,5515 \text{ kg m}^{-2} \text{ s}^{-1} \\ T_2 = 480 \text{ K} \\ \varphi_2 = 1.999\,9991 \\ H = G = 0 \\ Q_2 = -4.35 \times 10^{14} \text{ J} \end{array}\right\} \xi = -\infty.$$

Here the integration is reversed from a fixed state $k = 2$ to a new state 1. Figures 5 and 6 represent the structure of the condensation wave admitted by the solution of the equations described with $k = 2$. The structure is nearly identical to that of evaporation, except the direction of integration is reversed. With a suitable value for the heat of condensation Q, the integration begins from a vapour state to a liquid side through a thin region of phase front of order ten nanometres.

The density profile in figure 5 resembles an experimental observation of fuel-droplet condensation; the end state density is about 675 kg m^{-3}, prototypical of hydrocarbon liquid fuel [12, 9]. While the reverse heat is added to drive the vapour state back to a liquid, the far end state temperature gradients remain uniform such that $T(-\infty)$ is constant and $T(+\infty)$ is linearly decreasing with respect to ξ.

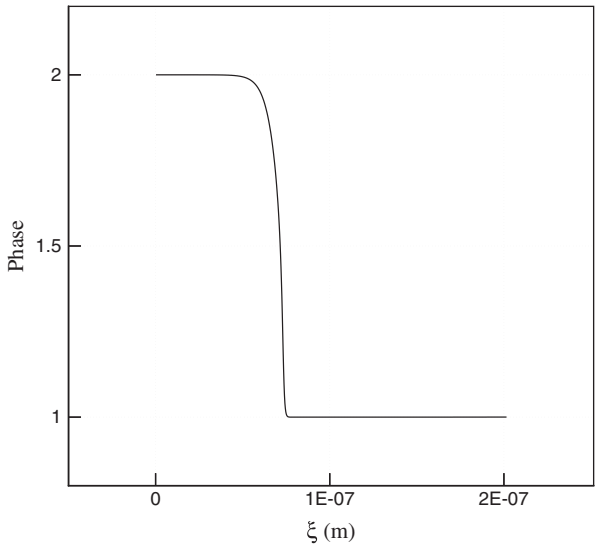

Figure 6. Condensation wave (vapour $\varphi = 2 \rightarrow$ liquid $\varphi = 1$) structure based on the phase field of n-heptane.

4.2. Melting and freezing front ($0 < \varphi < 1$)

The structure equations in the case of solid to liquid or liquid to solid transition are obtained in analogy to the evaporation–condensation case. The main distinction in the equations is the added dependence of conservative variables on the deformation field. A variable F is the one-dimensional deformation gradient which is introduced into the momentum, energy, and phase-field equations. Again with mass flux remaining a constant m, the momentum structure equation, after being integrated from $-\infty$ to a position in ξ, becomes

$$\frac{\mathrm{d}U}{\mathrm{d}\xi} = \frac{3}{4\mu_f}\left\{mU + p + \rho\gamma_\varphi G^2 - \mu_s F + \mu_l F^{-\frac{1}{1-2\nu_s}} - mU_k - p_k\right\} \tag{17}$$

where the equation of state and the thermal expansion terms of the general stress constitutive equation are absorbed into an effective pressure, p. If k is set to unity the equation represents melting, and if $k = 2$ the equation represents freezing. As for the energy equation, we have

$$\frac{\mathrm{d}H}{\mathrm{d}\xi} = \frac{1}{\kappa}\left\{mc_v H - \frac{4}{3}\mu_f\left(\frac{\mathrm{d}U}{\mathrm{d}\xi}\right)^2 + \left(\rho RT + \alpha_c\kappa F^{-1}T\right)\frac{\mathrm{d}U}{\mathrm{d}\xi} - B_\varphi(UG)^2 - \rho T\beta'_m(\varphi)\frac{Q_m}{T_m}UG + \beta'_m(\varphi)Q_k\right\} \tag{18}$$

where, as in the evaporation–condensation case, a new variable H is used ($H = \frac{\mathrm{d}T}{\mathrm{d}\xi}$), which is then solved together with equation (18). The specific heat c_v is assumed constant as before. The phase field equation reads

$$\frac{\mathrm{d}G}{\mathrm{d}\xi} = \frac{1}{\gamma_\varphi}\left\{UB_\varphi G + \frac{1}{2}\Psi\frac{\partial}{\partial\varphi}\{(\varphi(\varphi-1)(\varphi-2))^2\} + \beta'_m(\varphi)\frac{T-T_m}{T_m}Q_m + \mu'_s\frac{1}{2}F^{-1}(F^2-1) + \mu'_c\frac{1-2\nu_s}{2\nu_s}F^{-1}(F^{-\frac{2\nu_s}{1-2\nu_s}}-1) + \mu'_l\frac{3}{2}F^{-1/3}\right\}. \tag{19}$$

Lastly, we need to close the system with an additional equation which relates the deformation gradient with the velocity field via the identity $\frac{\mathrm{d}F}{\mathrm{d}\xi} = -\frac{F}{U_k}\frac{\mathrm{d}U}{\mathrm{d}\xi}$ or $F = \mathrm{e}^{-\frac{U}{U_k}+1}$.

Table 2. Dimensional parameters for HMX melting/freezing.

Property	Units	Value
Specific heat—solid, c_v^{sol}	J kg^{-1} K^{-1}	1.06×10^3 [a]
Specific heat—liquid, c_v^{liq}	J kg^{-1} K^{-1}	2.1×10^3 [b]
Gas constant per unit mass, R_{sol}	J kg^{-1} K^{-1}	1.1 [b]
Gas constant per unit mass, R_{liq}	J kg^{-1} K^{-1}	3.0 [b]
Thermal expansion coefficient, α_{sol}	1/K	0.000 134 [a]
Thermal conductivity, κ	W m^{-1} K^{-1}	0.36 [a]
Viscosity coefficient, μ_f	kg m^{-1} s^{-1}	1.0×10^{-3} [c]
Shear modulus—solid, μ_{sol}	GPa	2.46 [b]
Shear modulus—liquid, μ_{liq}	GPa	2.37 [b]
Poisson's ratio, ν_s		0.414 [c]
Multiplication factor of $\dot{\varphi}$, B_φ	kg m^{-1} s^{-1}	3.5×10^{-2} [b]
Phase diffusion coefficient, γ_φ	m kg s^{-2}	2.0×10^{-12} [b]
Depth of phase well, Ψ	J kg^{-1}	40.0×10^{-6} [b]
Melting temperature, T_m	K	558.0 [c]

[a] Reference [23].
[b] Modelled.
[c] LLNL Hand Book of Explosives, 1985.

For illustration of the melting and freezing front structure, we use HMX as the candidate for solid–liquid structure analysis for which a handful of material data are known [15–19]. Table 2 lists the parameters of HMX as needed in the calculation of melting and freezing structure. In the case of melting, the solid state of HMX is fixed by the following initial conditions at $\xi = -\infty$ with $k = 1$:

$$\left.\begin{aligned} &\rho_1 = 2000 \text{ kg m}^{-3} \\ &m = 2.0 \times 10^3 \text{ kg m}^{-2} \text{ s}^{-1} \\ &D = 1.0 \text{ m s}^{-1} \\ &u_1 = 0 \text{ m s}^{-1} \\ &T_1 = 300 \text{ K} \\ &p_1 = 6.075\,00 \times 10^5 \text{ Pa} \\ &\varphi_1 = 0.000\,0001 \\ &F = 1.000\,000\,01 \\ &H = G = 0 \\ &Q_1 = +3.3 \times 10^{14} \text{ J} \end{aligned}\right\} \xi = -\infty.$$

Since there are no data known for the melting rate of HMX, the value of D is assumed to be in the range of 10^{-3}–10^3 m s^{-1}. The minimum in this range corresponds to a typical deflagration rate while the maximum represents a typical detonation speed [20]. A natural choice is to take the mean value, approximately 1 m s^{-1}.

Figures 7–9 depict the structure of a melting front admitted by the equations. In particular, the initial density of 2000 kg m^{-3}, typical of solid explosive, decreases by a factor of two. The system of ODEs of melting is integrated from a slightly perturbed initial state into a new state representing a melt HMX. The thickness of the phase front is on the order of microns, supporting the observation that the explosive melting front is approximately 100 times thicker than the evaporation–condensation front of liquid fuel.

The initial state of solid HMX is unstressed (i.e. $F = 1$) while the end state of the integration is at a compression state at $F \sim 0.3$. In fact, the wave, a compression wave, on the far right side, propagates into an unstressed material on the left side at a steady melting

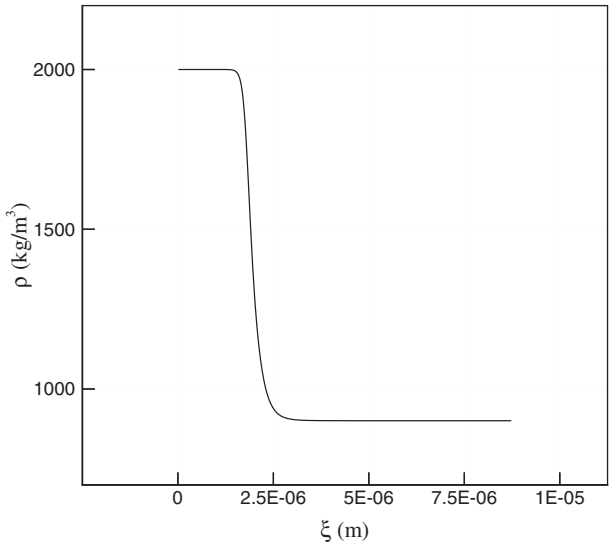

Figure 7. Melting front (solid $\varphi = 0 \rightarrow$ liquid $\varphi = 1$) structure observed from the transformed density field of solid HMX.

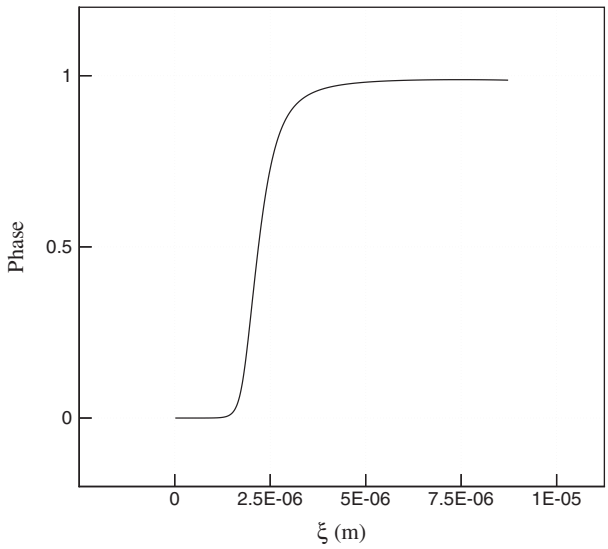

Figure 8. Melting front (solid $\varphi = 0 \rightarrow$ liquid $\varphi = 1$) structure observed from the transformed phase field of solid HMX.

speed of D. This observation is consistent with the principle of energy transfer from a higher state to a lower state. The temperature field also supports this observation that the uniform state on the left is balanced by a linearly increasing thermal field (i.e. a thicker temperature transition region) on the far right, causing the energy transfer to go from a liquid to a solid, essentially a melting process [21, 22, 17].

In the case of freezing, liquid state 2 is fixed at $-\infty$, and the integration starts from the far left in the liquid region to a solid state at $+\infty$. Listed below are the initial conditions of

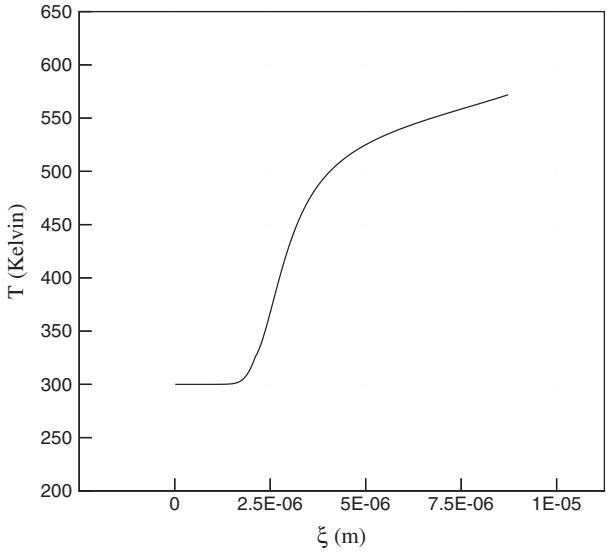

Figure 9. Melting front (solid $\varphi = 0 \rightarrow$ liquid $\varphi = 1$) structure observed from the transformed temperature field of solid HMX.

integration for which the liquid state is assumed uniform:

$$\left.\begin{aligned} &\rho_2 = 1580 \text{ kg m}^{-3} \\ &U_2 = 1.4 \text{ m s}^{-1} \\ &m = 2.0 \times 10^3 \text{ kg m}^{-2} \text{ s}^{-1} \\ &T_2 = 700 \text{ K} \\ &\varphi_2 = 0.999\,999\,91 \\ &F = 1.000\,000\,01 \\ &H = G = 0 \\ &Q_2 = -4.2 \times 10^{14} \text{ J} \end{aligned}\right\} \xi = -\infty.$$

Figures 10 and 11 represent the structure of a freezing front, admitted by the equations by setting $k = 2$. Previous investigation of thermodynamic properties of HMX suggests that the material can undergo a liquid–solid transition at a temperature 550 K and a pressure above 50×10^5 Pa. So the process of 'freezing', in principle, is attainable at this melting temperature with an elevated pressure of 50×10^5 Pa or above. Typical melt explosive of density 10^3 kg m^{-3} makes a rapid transition to a new state, a solid state as shown in figure 10. Again, the thickness of the numerically obtained freezing front is on the order of microns, which is about 100 times the thickness of the condensation front of hydrocarbon liquid fuel. As the phase variable changes from unity to zero, the deformation field goes from an unstressed liquid at $F(-\infty) \approx 1$ to a tensional state at $F(+\infty) \approx 1.3$. The front again moves from right to left with a steady propagating speed of $D \approx 1.26$ m s^{-1}.

5. Conclusion

A thermo-mechanical model for energetic materials that undergo phase transformations is reconstructed for understanding the structure of waves associated with combustion phenomena. In particular, the thickness of evaporation and condensation phase fronts are analysed by

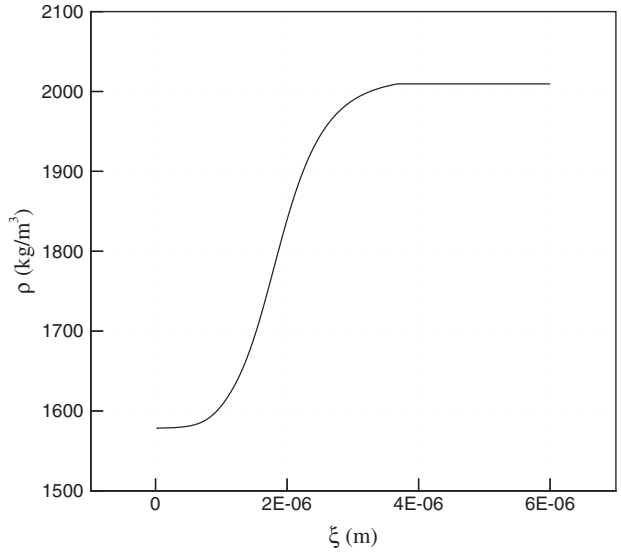

Figure 10. Freezing front (liquid $\varphi = 1 \rightarrow$ solid $\varphi = 0$) structure observed from the transformed density field of liquid HMX.

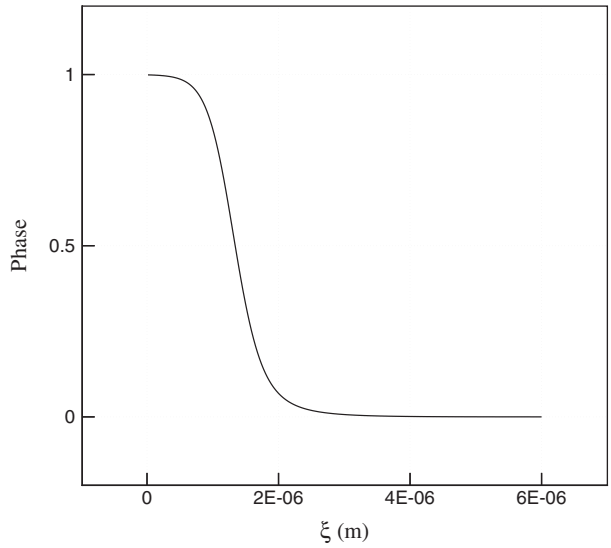

Figure 11. Freezing front (liquid $\varphi = 1 \rightarrow$ solid $\varphi = 0$) structure observed from the transformed phase field of liquid HMX.

integrating the structure equations of n-heptane from one state to the other. The thickness estimation of melting and freezing waves is illustrated by considering HMX as an energetic material undergoing phase transformation. Based on the analysis, the phase front width of liquid–gas or gas–liquid phase (of, say, a liquid fuel) is approximately one-100th of the calculated width of the solid–liquid or liquid–solid phase front of a high explosive. Though not fully generalized at this stage, the approach illustrated in this paper can be extended to phase front thickness estimations of a condensed matter whose front thickness measurement

is not experimentally attainable. Other use of this technique may include size estimation of a small scale device where melting and evaporation of liquid and solid fuels exist during the normal operation of the device. Currently, additional candidate energetic materials are studied for their phase front structure by extending the wavefront integration technique as discussed in this work.

Acknowledgments

The author acknowledges the support from the BK 21 Project through the Institute of Advanced Aerospace Technology at the Seoul National University. Partial support from the Korea Research Foundation through grant No KRF-2005-003-D00057 is also warmly acknowledged. Discussions with D Scott Stewart of UIUC are also deeply appreciated.

Appendix

$$
\begin{aligned}
\beta'_m(\varphi) &= \begin{cases} 6\varphi(1-\varphi) & \text{for } 0 \leqslant \varphi \leqslant 1 \\ 0 & \text{otherwise} \end{cases} \\
\beta'_v(\varphi) &= \begin{cases} 6(\varphi-1)(2-\varphi) & \text{for } 1 \leqslant \varphi \leqslant 2 \\ 0 & \text{otherwise} \end{cases} \\
\mu_c(\varphi) &= \begin{cases} 2(\mu_{\mathrm{sol}}-\mu_{\mathrm{liq}})\varphi^3 - 3(\mu_{\mathrm{sol}}-\mu_{\mathrm{liq}})\varphi^2 + \mu_{\mathrm{sol}} & \text{for } 0 \leqslant \varphi \leqslant 1 \\ 2(\mu_{\mathrm{liq}})(\varphi-1)^3 - 3(\mu_{\mathrm{liq}})(\varphi-1)^2 + \mu_{\mathrm{liq}} & \text{for } 1 \leqslant \varphi \leqslant 2 \end{cases} \\
\mu'_c(\varphi) &= \begin{cases} 6(\mu_{\mathrm{sol}}-\mu_{\mathrm{liq}})\varphi^2 - 6(\mu_{\mathrm{sol}}-\mu_{\mathrm{liq}})\varphi & \text{for } 0 \leqslant \varphi \leqslant 1 \\ 6(\mu_{\mathrm{liq}})(\varphi-1)^2 - 6(\mu_{\mathrm{liq}})(\varphi-1) & \text{for } 1 \leqslant \varphi \leqslant 2 \end{cases} \\
\mu_s(\varphi) &= \begin{cases} 2(\mu_{\mathrm{sol}})\varphi^3 - 3(\mu_{\mathrm{sol}})\varphi^2 + \mu_{\mathrm{sol}} & \text{for } 0 \leqslant \varphi \leqslant 1 \\ 0 & \text{for } \varphi > 1 \end{cases} \\
\mu'_s(\varphi) &= \begin{cases} 6(\mu_{\mathrm{sol}})\varphi^2 - 6(\mu_{\mathrm{sol}})\varphi & \text{for } 0 \leqslant \varphi \leqslant 1 \\ 0 & \text{otherwise} \end{cases} \\
\mu_l(\varphi) &= \begin{cases} 2(-\mu_{\mathrm{liq}})\varphi^3 - 3(-\mu_{\mathrm{liq}})\varphi^2 & \text{for } 0 \leqslant \varphi \leqslant 1 \\ 2(\mu_{\mathrm{liq}})(\varphi-1)^3 - 3(\mu_{\mathrm{liq}})(\varphi-1)^2 + \mu_{\mathrm{liq}} & \text{for } 1 \leqslant \varphi \leqslant 2 \end{cases} \\
\mu'_l(\varphi) &= \begin{cases} 6(-\mu_{\mathrm{liq}})\varphi^2 - 6(-\mu_{\mathrm{liq}})\varphi & \text{for } 0 \leqslant \varphi \leqslant 1 \\ 6(\mu_{\mathrm{liq}})(\varphi-1)^2 - 6(\mu_{\mathrm{liq}})(\varphi-1) & \text{for } 1 \leqslant \varphi \leqslant 2 \end{cases} \\
R(\varphi) &= \begin{cases} 2(-R_{\mathrm{vap}})(\varphi-1)^3 - 3(-R_{\mathrm{vap}})(\varphi-1)^2 & \text{for } 1 \leqslant \varphi \leqslant 2 \\ 0 & \text{for } \varphi < 1 \end{cases} \\
R'(\varphi) &= \begin{cases} 6(-R_{\mathrm{vap}})(\varphi-1)^2 - 6(-R_{\mathrm{vap}})(\varphi-1) & \text{for } 1 \leqslant \varphi \leqslant 2 \\ 0 & \text{otherwise} \end{cases} \\
\alpha_c(\varphi) &= \begin{cases} 2(\alpha_{\mathrm{sol}})(\varphi-1)^3 - 3(\alpha_{\mathrm{sol}})(\varphi-1)^2 & \text{for } 1 \leqslant \varphi \leqslant 2 \\ \alpha_{\mathrm{sol}} & \text{for } \varphi < 1 \end{cases} \\
\alpha'_c(\varphi) &= \begin{cases} 6(\alpha_{\mathrm{sol}})(\varphi-1)^2 - 6(\alpha_{\mathrm{sol}})(\varphi-1) & \text{for } 1 \leqslant \varphi \leqslant 2 \\ 0 & \text{otherwise} \end{cases} \\
\rho\gamma_\varphi(\varphi) &= \begin{cases} 6(-\rho\gamma_\varphi)\varphi^2 - 6(-\rho\gamma_\varphi)\varphi & \text{for } 0 \leqslant \varphi \leqslant 1 \\ 6(-\rho\gamma_\varphi)(\varphi-1)^2 - 6(-\rho\gamma_\varphi)(\varphi-1) & \text{for } 1 \leqslant \varphi \leqslant 2 \end{cases} \\
c_v(\varphi) &= c_v
\end{aligned}
$$

References

[1] Elizarova T G, Shirokov I A and Montero S 2005 Numerical simulation of shock-wave structure for argon and helium *Phys. Fluids* **17** 068101

[2] Greywall M S 1975 Thickness of an embedded ion shock *Phys. Fluids* **18** 1439–42

[3] Uribe F J, Velasco R M, Garcia-Colin L S and Diaz-Herrera E 2000 Shock wave profiles in the burnett approximation *Phys. Rev.* E **62** 6648–66

[4] Alsmeyer H 1976 Density profiles in argon and nitrogen shock waves measured by the absorption of an electron beam *J. Fluid Mech.* **74** 497–513

[5] Ruggeri T 1993 Breakdown of shock-wave-structure solutions *Phys. Rev.* E **47** 4135–40

[6] Yoh J J, Stewart D S and Ruderman G A 2002 A thermomechanical model for energetic materials with phase transformations: numerical simulations and examples for simple motions *SIAM J. Appl. Math.* **63** 538–63

[7] Ruderman G A, Stewart D S and Yoh J J 2002 A thermomechanical model for energetic materials with phase transformations *SIAM J. Appl. Math.* **63** 510–37

[8] Dick D R 1975 *Engineering Sciences Data Unit Index* Engineering Sciences Data Unit Ltd

[9] Timmermans J 1965 *Physico-Chemical Constants of Pure Organic Compounds* vol 1, 2 (Amsterdam: Elsevier)

[10] Yoh J J and Zhong X 2004 New hybrid Runge–Kutta methods for unsteady reactive flow simulation *AIAA J.* **42** 1593–600

[11] Sirignano W A 1999 *Fluid Dynamics and Transport of Droplets and Sprays* (Cambridge: Cambridge University Press)

[12] Law C K 1982 Recent advances in droplet vaporization and condensation *Prog. Energy Combust. Sci.* **88** 171–201

[13] Shuen J S, Yang V and Hsia C C 1992 Combustion of liquid-fuel droplets in supercritical conditions *Combust. Flame* **89** 299–319

[14] Thompson P A 1988 *Compressible-Fluid Dynamics* (*Advanced Engineering Series*) (New York: McGraw-Hill)

[15] Boggs T L 1984 The thermal behavior of cyclotrimethylenetrinitramine (RDX) and cyclotetramethylenetetranitramine (HMX) *Prog. Astro. Aero.* **90** 121–75

[16] Dobratz B M 1981 *LLNL Explosive Handbook* (California: Lawrence Livermore Laboratory)

[17] Poirier J-P 1991 *Introduction to the Physics of the Earth's Interior* (Cambridge: Cambridge University Press)

[18] Zinn J and Rogers R N 1962 Thermal initiation of explosives *J. Phys. Chem.* **66** 2646–53

[19] Yoh J J, McClelland M A, Maienschein J L, Nichols A L and Tarver C M 2006 Simulating thermal explosion of HMX-based explosives: model comparison with experiment *J. Appl. Phys.* at press

[20] Fickett W and Davis W C 1979 *Detonation* (Berkeley, CA: University of California Press)

[21] Pippard A B 1966 *Elements of Classical Thermodynamics for Advanced Students of Physics* (Cambridge: Cambridge University Press)

[22] Callen H B 1985 *Thermodynamics: an Introduction to the Physical Theories of Equilibrium Thermostatics and Irreversible Thermodynamics* (New York: Wiley)

[23] Menikoff R and Sewell T D 2002 *Combust. Theor. Model.* **6** 103–25